

# Transmission electron microscopy analysis of the crystallography of precipitates in Mg–Sn alloys aged at high temperatures

Xin Nie,<sup>a</sup> Yimin Guan,<sup>a</sup> Dongshan Zhao,<sup>a\*</sup> Yu Liu,<sup>b</sup> Jianian Gui,<sup>a</sup> Luying Li<sup>c</sup> and Jianbo Wang<sup>a</sup>

<sup>a</sup>School of Physics and Technology, Center for Electron Microscopy and MOE Key Laboratory of Artificial Micro- and Nano-structures, Wuhan University, Wuhan, Hubei 430072, People's Republic of China, <sup>b</sup>New Materials, Shandong Academy of Sciences, Jinan, Shandong 250014, People's Republic of China, and <sup>c</sup>Center for Nanoscale Characterization and Devices, Wuhan National Laboratory for Optoelectronics, Huazhong University of Science, Wuhan, Hubei 430074, People's Republic of China. Correspondence e-mail: dszhao@whu.edu.cn

The crystallographic orientation relationships (ORs) of precipitated  $\beta$ -Mg<sub>2</sub>Sn particles in Mg–9.76 wt% Sn alloy aged at 573 K for 5 h, corresponding to its peak hardness, were investigated by advanced transmission electron microscopy (TEM). OR-3 of  $(110)_{\beta}/(0001)_{\alpha}$  and  $[\bar{1}11]_{\beta}/[1\bar{2}10]_{\alpha}$  and OR-4 of  $(110)_{\beta}/(0001)_{\alpha}$  and  $[001]_{\beta}/[2\bar{1}\bar{1}0]_{\alpha}$  are the key ORs of  $\beta$ -Mg<sub>2</sub>Sn particles in the alloy. The proportions of  $\beta$ -Mg<sub>2</sub>Sn particles exhibiting OR-3 and OR-4 were determined as 75.1 and 24.3%, respectively. Crystallographic factors determined the predominance of OR-3 in the precipitated  $\beta$ -Mg<sub>2</sub>Sn particles. This mechanism was analyzed by a three-dimensional invariant line model constructed using a transformation matrix in reciprocal space. Models of the interface of precipitated  $\beta$ -Mg<sub>2</sub>Sn and the  $\alpha$ -Mg matrix were constructed *via* high-resolution TEM and atomic resolution high-angle annular dark-field scanning TEM.

© 2014 International Union of Crystallography

## 1. Introduction

Magnesium-based alloys are lightweight structural materials that have elicited great interest because of their ability to reduce the weight of automobiles (Luo, 2004; Nie, 2012; Yoon & Park, 2014). Among those alloys, Mg–Al-based alloys are widely used in many areas because of their superior castability and ideal mechanical behavior at room temperature (Celloto, 2000; Zheng *et al.*, 2009; Zhou *et al.*, 2007, 2009). However, Mg–Al alloys exhibit poor creep resistance at temperatures between 393 and 573 K because their secondary precipitate,  $\gamma$ -Mg<sub>17</sub>Al<sub>12</sub>, has a low melting point (735 K) and is a poor strengthening phase at high temperatures (Hort *et al.*, 2006). Mg–Sn-based alloys have recently been studied for their potential high-temperature applications (Kang *et al.*, 2005; Wei *et al.*, 2008). These alloys can be developed into precipitation-hardenable alloys according to their binary phase diagrams (Murray, 1997) because the maximum solid solubility of Sn in  $\alpha$ -Mg is 14.85 wt% at a eutectic temperature 834 K and decreases to 0.45 wt% at 473 K. The equilibrium volume fraction of Mg–10.0 wt% Sn alloy precipitated at 573 K is approximately 11.1%. These precipitates are the equilibrium phase of  $\beta$ -Mg<sub>2</sub>Sn, which has a face-centered cubic (f.c.c.) structure.

The  $\alpha$ -Mg matrix exhibits a hexagonal close-packed (h.c.p.) structure. The lattice parameters for the  $\beta$ -Mg<sub>2</sub>Sn phase and  $\alpha$ -Mg matrix are  $a_{\beta} = 6.759$  Å (space group  $Fm\bar{3}m$ ; JCPDS 65-

2997) and  $a_{\alpha} = 3.209$ ,  $c_{\alpha} = 5.210$  Å (space group  $P6_3/mmc$ ; JCPDS 89-5003), respectively. Liu *et al.* (2007) analyzed as-cast Mg–(1–10) wt% Sn alloys and suggested that the Mg–5 wt% Sn alloy exhibits the best ductility and creep resistance, whereas the Mg–10 wt% Sn alloy manifests the highest hardness. Van der Planken (1969) found that the time required by Mg–7.75 wt% Sn alloys aged at 473, 523 and 573 K to reach their peak hardness decreases with increasing temperature. Mendis *et al.* (2006a) revealed that the morphology, orientation relationships (ORs), and unit volume density of precipitates of Mg–6 wt% Sn-based alloys markedly affect their properties after annealing and aging at 473 K to peak hardness. Derge *et al.* (1937) examined the ORs between the  $\beta$ -Mg<sub>2</sub>Sn phase and  $\alpha$ -Mg matrix using X-ray diffractometry and optical microscopy and reported that the  $\beta$ -Mg<sub>2</sub>Sn phase presents a plate-like morphology (Table 1). According to Henes & Gerold (1962), the  $\beta$ -Mg<sub>2</sub>Sn phase in an Mg–Sn alloy exhibited OR-1 and OR-2 at temperatures between 473 and 573 K, and exhibited OR-3 and OR-4 at temperatures between 403 and 473 K (Table 1). The frequencies of these ORs and their precise morphologies, however, remain unknown, and information on Mg–Sn alloys remains unclear despite the availability of related studies. Zhang *et al.* (2007), Sasaki *et al.* (2006) and Shi *et al.* (2012) reported the OR-5, OR-6, OR-7 and OR-8 forms of the  $\beta$ -Mg<sub>2</sub>Sn phase (Table 1). The presence of several ORs and the influence of crystal-

**Table 1**

Reported ORs and morphologies between a precipitated  $\beta$ -Mg<sub>2</sub>Sn particle (f.c.c.) and the  $\alpha$ -Mg matrix (h.c.p.) in Mg–Sn systems.

Name	OR-1	OR-2	OR-3	OR-4
OR	$(111)_\beta // (0001)_\alpha [1\bar{1}0]_\beta // [2\bar{1}\bar{1}0]_\alpha$	$(111)_\beta // (0001)_\alpha [2\bar{1}\bar{1}]_\beta // [2\bar{1}\bar{1}0]_\alpha$	$(110)_\beta // (0001)_\alpha [\bar{1}11]_\beta // [1\bar{2}10]_\alpha$	$(110)_\beta // (0001)_\alpha [001]_\beta // [2\bar{1}\bar{1}0]_\alpha$
Morphology	Lath shaped, plate shaped and polygon shaped	Lath shaped and plate shaped	Lath shaped and plate shaped	Lath shaped
References	Derge <i>et al.</i> (1937); Henes & Gerold (1962); Kang <i>et al.</i> (2007); Mendis <i>et al.</i> (2006a,b); Sasaki <i>et al.</i> (2006, 2011); Zhang <i>et al.</i> (2007)	Derge <i>et al.</i> (1937); Henes & Gerold (1962); Sasaki <i>et al.</i> (2011)	Derge <i>et al.</i> (1937); Henes & Gerold (1962); Mendis <i>et al.</i> (2006b); Sasaki <i>et al.</i> (2006, 2011)	Henes & Gerold (1962); Sasaki <i>et al.</i> (2009); Zhang <i>et al.</i> (2007)

Name	OR-5	OR-6	OR-7	OR-8
OR	$(111)_\beta // (0001)_\alpha, [2\bar{1}\bar{1}0]_\alpha$ 9° from $[110]_\beta$	$(111)_\beta // (01\bar{1}0)_\alpha [1\bar{1}0]_\beta // [2\bar{1}\bar{1}0]_\alpha$	$(110)_\beta // (0001)_\alpha [1\bar{1}1]_\beta // [01\bar{1}0]_\alpha$	$(110)_\beta // (0001)_\alpha [001]_\beta // [01\bar{1}0]_\alpha$
Morphology	Plate shaped	Lath shaped	Lath shaped	Lath shaped
References	Zhang <i>et al.</i> (2007)	Sasaki <i>et al.</i> (2011)	Shi <i>et al.</i> (2012)	Shi <i>et al.</i> (2012)

lographic factors on their formation have yet to be determined.

In this paper, the ORs and interface structures of the  $\beta$ -Mg<sub>2</sub>Sn phase in an Mg–9.76 wt% Sn alloy were analyzed using high-resolution transmission electron microscopy (HRTEM) and high-angle annular dark-field scanning TEM (HAADF-STEM).

## 2. Experimental

Ingots of as-cast Mg–9.76 wt% Sn alloy were prepared and cut into bars/slices by electrical discharge machining. The resultant bars/slices were initially heat treated at 823 K for 12 h under the protection of argon flow to dissolve the  $\beta$ -Mg<sub>2</sub>Sn phase and achieve a homogeneous tin distribution. Subsequently, these samples were immediately quenched in water. All of the alloys were aged at 573 K in a muffle furnace for various aging times immediately after annealing. Age hardening responses were measured at the internal regions of  $\alpha$ -Mg grains using a micro-Vickers hardness tester (HXD-1000TMC/LCD) under a load of 1 kg. Each hardness value is reported as the average of at least six individual measurements. The overall phase structures of the test alloys were analyzed using X-ray diffractometry (XRD) and scanning electron microscopy (SEM). XRD was performed on a Bruker AXS D8 Advance X-ray diffractometer with Cu  $K\alpha$  radiation ( $\lambda = 0.1542$  nm). SEM observations were carried out on a SIRON TMP field-emission scanning electron microscope equipped with an EDAX energy dispersive X-ray spectrometer. The SEM samples were mechanically polished and then etched with a solution of 5 vol% nitric acid + absolute ethanol prior to characterization. The alloy slices were mechanically thinned to approximately 50  $\mu$ m, and 3 mm-wide discs were punched and electrochemically polished. The alloy specimens were then ion milled using a Gatan precision ion polishing system (operating voltage, 3.0 kV). Conventional TEM was conducted using a JEOL JEM-2010 (HT) (high-angle tilt) microscope (LaB<sub>6</sub> gun) operated at a voltage of 200 kV. High-resolution TEM and energy dispersive X-ray spectroscopy (EDS) analysis of the same specimen were performed on a

JEOL JEM-2010 FEF (UHR) electron microscope with a field emission gun and an in-column  $\Omega$ -type energy filter operated at 200 kV. The JEM-2010 FEF instrument was coupled to an EDAX energy dispersive X-ray spectrometer and a Gatan Model-894 CCD digital camera. Aberration-corrected HAADF-STEM images were acquired using an FEI Titan G2 60-300 transmission electron microscope (Prob Cs Corrector UHRSTEM) at an accelerating voltage of 300 kV.

## 3. Results and discussion

Ingots of as-cast Mg–9.76 wt% Sn alloy were heat treated at 823 K for 12 h until completely dissolved and then aged at 573 K. Fig. 1 shows that the hardness of the samples rapidly increases, reaching a maximum (63.5 HV) at 5 h and then gradually decreasing with further increases in time. The peak hardness and aging time of the present alloy were similar to those of Mg–7.75 wt% Sn alloys (60 HV and about 5 h) obtained after annealing and aging at 823 and 573 K, respectively (Van der Planken, 1969).

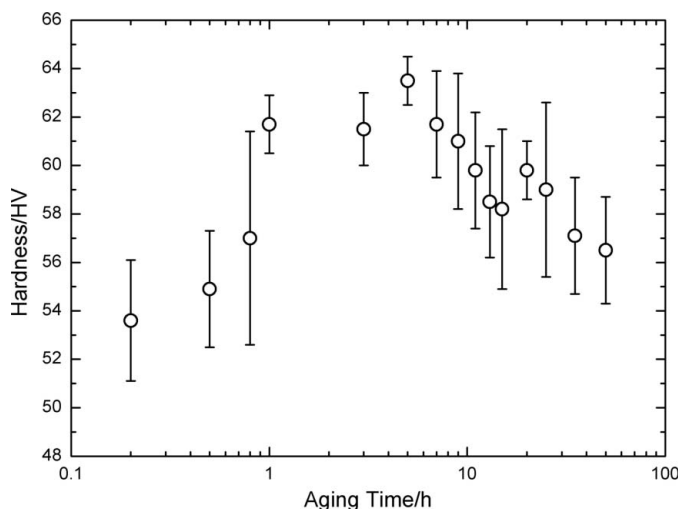


**Figure 1** Age hardening curve of the as-cast Mg–9.76 wt% Sn alloy aged at 573 K after annealing at 823 K for 12 h.

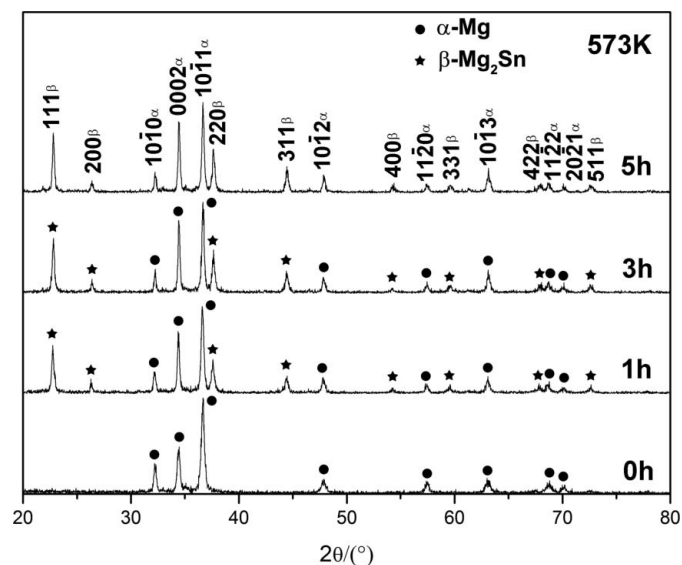
Fig. 2 shows the powder XRD patterns of supersaturated Mg–9.76 wt% Sn alloys annealed at 573 K for 0, 1, 3 and 5 h. All of the XRD peaks could be indexed to either an  $\alpha$ -Mg structure with lattice parameters of  $a_\alpha = 3.198$ ,  $c_\alpha = 5.201$  Å or a  $\beta$ -Mg<sub>2</sub>Sn structure with a lattice parameter of  $a_\beta = 6.747$  Å. The peak aging time (5 h) was investigated to correlate the hardness of the sample alloys with the microstructures formed. Fig. 3(a) shows the SEM secondary electron image of the supersaturated Mg–9.76 wt% Sn alloy before aging. Figs. 3(b) and 3(c) show different magnifications of SEM secondary electron images of the supersaturated Mg–9.76 wt% Sn alloy aged at 573 K for 5 h to peak hardness. The results show that the precipitated  $\beta$ -Mg<sub>2</sub>Sn particles are densely distributed in the internal region of the  $\alpha$ -Mg grains. The dark areas marked by arrows in Fig. 3(b) correspond to the  $\beta$ -Mg<sub>2</sub>Sn phase formed in the boundary regions of  $\alpha$ -Mg grains. Fig. 3(c) illustrates the internal area of an  $\alpha$ -Mg grain [white square in Fig. 3(b)]. Most of the precipitated  $\beta$ -Mg<sub>2</sub>Sn particles with bright contrast exhibit complicated lath-shaped morphologies. Typical  $\beta$ -Mg<sub>2</sub>Sn particles are indicated by arrows in Fig. 3(c).

Fig. 4(a) shows a bright-field TEM image of the pre-aged Mg–9.76 wt% Sn alloy, and Fig. 4(b) shows the corresponding selected area electron diffraction (SAED) pattern. Figs. 4(a) and 4(b) indicate that the total dissolution of the  $\beta$ -Mg<sub>2</sub>Sn phase was achieved after heat treatment at 823 K for 12 h and confirm the XRD results in Fig. 2 and the SEM result in Fig. 3(a). Fig. 4(c) shows a bright-field TEM image taken along the  $[2\bar{1}\bar{1}0]_\alpha$  direction of the Mg–9.76 wt% Sn alloy aged at 573 K for 5 h to peak hardness. Tilting and SAED results confirm that the precipitated particles [marked as P<sub>1</sub>, P<sub>2</sub> and P<sub>3</sub>; Fig. 4(c)] of the  $\beta$ -Mg<sub>2</sub>Sn phase with OR-4 were platelet like (thickness 60 nm) along the  $[0001]_\alpha$  direction of the  $\alpha$ -Mg matrix. Figs. 4(d) and 4(f), respectively, reveal the corresponding SAED patterns of P<sub>1</sub> and the matrix along the  $[001]_\beta/[2\bar{1}\bar{1}0]_\alpha$  and  $[1\bar{1}0]_\beta/[01\bar{1}0]_\alpha$  directions. Figs. 4(e) and 4(g) show simulated electron diffraction patterns based on the

kinematic diffraction theory, which correspond to the real images of Figs. 4(d) and 4(f), respectively.

A typical particle Q<sub>1</sub> (Fig. 4c) of the  $\beta$ -Mg<sub>2</sub>Sn phase with OR-3 exhibited platelets (length 600 nm, thickness 25 nm). The corresponding SAED and kinematically simulated electron diffraction patterns of Q<sub>1</sub>, Q<sub>2</sub>, Q<sub>3</sub>, Q<sub>4</sub> and Q<sub>5</sub> along the  $[\bar{1}11]_\beta/[1\bar{2}10]_\alpha$  direction are shown in Figs. 4(h) and 4(i), respectively. The results suggest that these particles exhibit an OR of OR-3 with the  $\alpha$ -Mg matrix. Figs. 4(j) and 4(k), respectively, show a bright-field TEM image and the corresponding SAED pattern taken along the  $[0001]_\alpha$  direction of the  $\alpha$ -Mg matrix for the Mg–9.76 wt% Sn alloy aged at 573 K for 5 h.  $\beta$ -Mg<sub>2</sub>Sn particles marked as Q<sub>6</sub>, Q<sub>7</sub>, Q<sub>8</sub>, Q<sub>9</sub>, Q<sub>10</sub>, Q<sub>11</sub>, Q<sub>12</sub> and Q<sub>13</sub> were identified to be of OR-3, while those marked as P<sub>4</sub> and P<sub>5</sub> were associated with OR-4 (Fig. 4j). The growth direction of  $\beta$ -Mg<sub>2</sub>Sn particles with OR-3 was parallel to the  $\langle 1\bar{1}2 \rangle_\beta / \langle 10\bar{1}0 \rangle_\alpha$  direction. The angle between the growth directions of  $\beta$ -Mg<sub>2</sub>Sn particles with OR-3 (Q<sub>6</sub>, Q<sub>7</sub> and Q<sub>8</sub>) was 120° (Fig. 4j). The growth direction of the  $\beta$ -Mg<sub>2</sub>Sn particle with OR-4 (P<sub>4</sub>) was parallel to the  $[001]_\beta/[2\bar{1}\bar{1}0]_\alpha$  direction (Fig. 4j). The growth directions of the  $\beta$ -Mg<sub>2</sub>Sn particles with OR-3 and OR-4 are in agreement with those reported by Zhang *et al.* (2007). In Fig. 4(j), a typical particle Q<sub>7</sub> of the  $\beta$ -Mg<sub>2</sub>Sn phase with OR-3 shows platelets with dimensions of 380 nm length and 70 nm width, and a  $\beta$ -Mg<sub>2</sub>Sn particle P<sub>5</sub> with OR-4 shows platelets with dimensions of 260 nm length and 55 nm width.

With the obtained lattice parameters for the  $\alpha$ -Mg matrix and  $\beta$ -Mg<sub>2</sub>Sn phase in Fig. 2, the stereographic projections of OR-1–OR-8 were calculated as shown in Figs. 5(a)–5(h),



**Figure 2**  
XRD patterns of as-cast Mg–9.76 wt% Sn alloys aged for different times at 573 K after annealing at 823 K for 12 h.

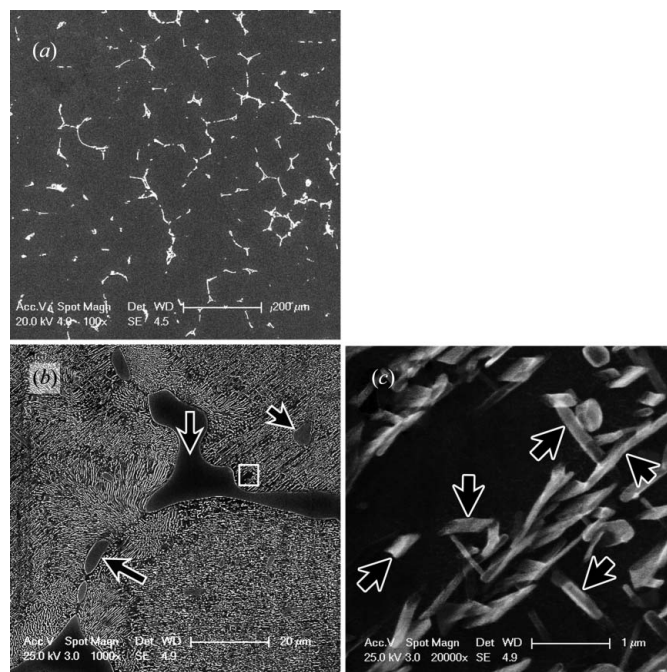


**Figure 3**  
(a) SEM secondary electron images of as-cast Mg–9.76 wt% Sn alloys aged (a) for 0 h and (b) at 573 K for 5 h after annealing at 823 K for 12 h. (c) Magnified SEM secondary electron image corresponding to the area marked by a white square in (b).

respectively. In Fig. 5, the thin lines indicate the plane traces of the  $\alpha$ -Mg matrix, and the directions marked by  $h_1$ – $h_8$  represent  $[03\bar{3}1]$ ,  $[03\bar{3}2]$ ,  $[01\bar{1}1]$ ,  $[02\bar{2}3]$ ,  $[01\bar{1}2]$ ,  $[11\bar{2}1]$ ,  $[22\bar{4}3]$  and  $[11\bar{2}3]$ , respectively. In Fig. 5, the thick lines represent plane traces of the  $\beta$ -Mg<sub>2</sub>Sn phase, and the directions marked by  $B_1$ – $B_3$  correspond to  $[100]$ ,  $[1\bar{1}0]$  and  $[1\bar{1}1]$ , respectively. When the  $\beta$  lattice is rotated clockwise at about  $5.23^\circ$  around the  $[0001]_\alpha$  direction while retaining the condition of  $[0002]_\alpha//[220]_\beta$  or  $(0002)_\alpha/(220)_\beta$ , OR-3 could be reached from OR-4 based on a comparison of Figs. 5(c) and 5(d).

Three crystallographic ORs (OR-1, OR-3 and OR-4) were observed *via* SAED and tilting techniques. Table 2 lists the statistical results of the crystallographic ORs of 334  $\beta$ -Mg<sub>2</sub>Sn particles of Mg–9.76 wt% Sn alloy aged at 573 K for 5 h. About 75.1 and 24.3% of the  $\beta$ -Mg<sub>2</sub>Sn particles exhibited OR-

**Table 2**

Statistical survey of the ORs and morphologies of precipitated  $\beta$ -Mg<sub>2</sub>Sn particles in the Mg–9.76 wt% Sn alloy aged at 573 K for 5 h.

Length range of the long axis of lath-shaped particles of $\beta$ -Mg <sub>2</sub> Sn (nm)	Number of lath-shaped particles with OR-1	Number of lath-shaped particles with OR-3	Number of lath-shaped particles with OR-4
<100	0	5	8
100–200	0	43	25
200–500	1	134	40
500–1000	0	53	8
>1000	1	16	0
Sum of the above	2	251	81

3 and OR-4, respectively. OR-3 was formed by most of the particles of the  $\beta$ -Mg<sub>2</sub>Sn phase in the alloy with the  $\alpha$ -Mg matrix (Table 2, and Figs. 4c and 4j).

To elucidate the statistical results (Table 2) in terms of a three-dimensional invariant line model (Zhang & Purdy, 1993; Luo & Weatherly, 1987; Dahmen, 1982), the transformation matrices  $A_0$  in real space and  $A_0'^{-1}$  in reciprocal space ( $A_0'$  corresponding to the transposed matrix of  $A_0$ ) must be determined.  $A_0'^{-1}$  was determined under the condition that the base vectors of each phase are correlated by small displacements  $\Delta g$  in reciprocal space. The SAED patterns (Figs. 4d and 4f) reveal that three small noncoplanar  $\Delta g$  values must be

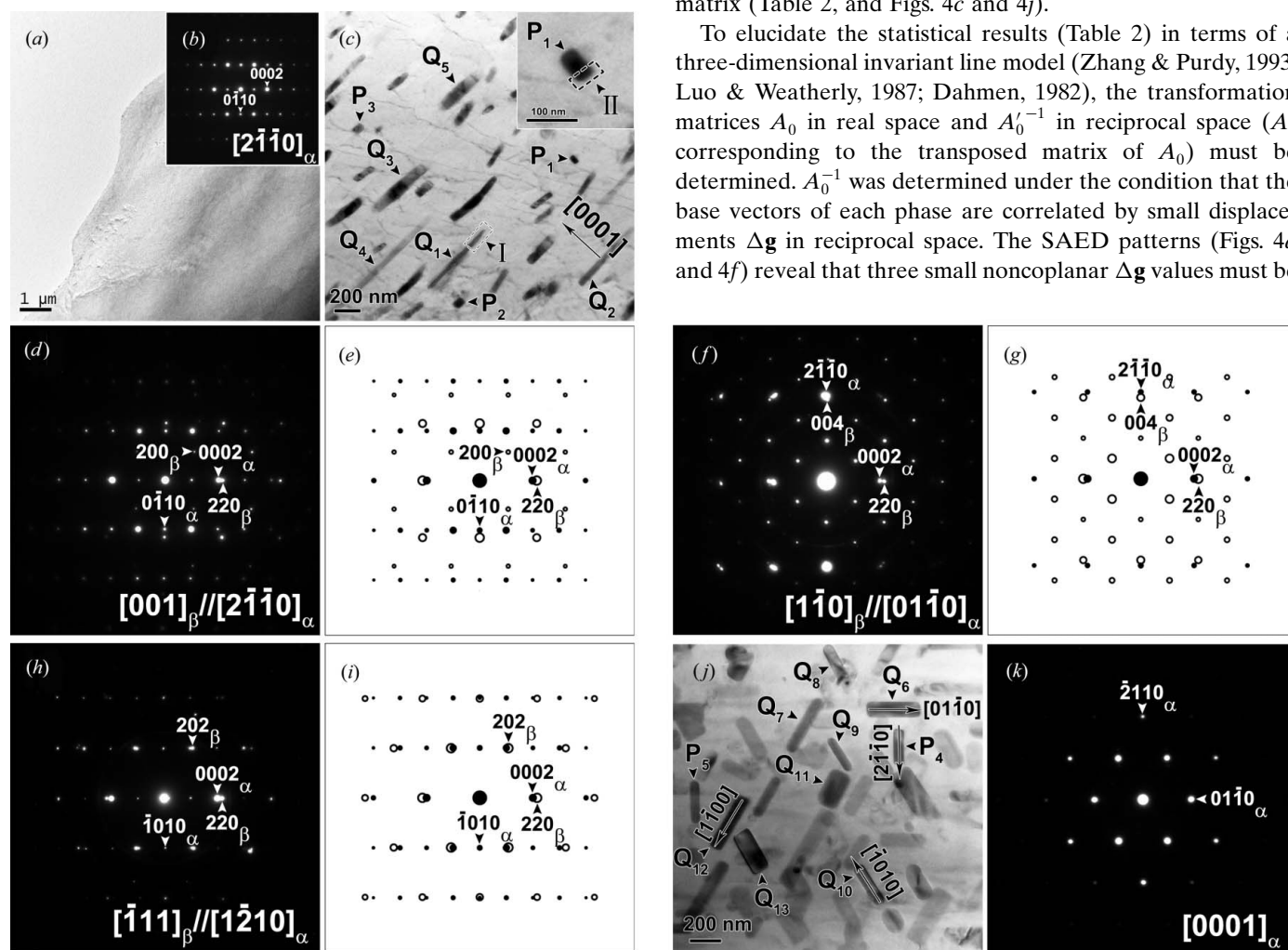


**Figure 4**

(a) TEM bright-field image of the as-cast Mg–9.76 wt% Sn alloy after annealing at 823 K for 12 h and before aging. (b) Corresponding SAED pattern obtained from the internal region of an  $\alpha$ -Mg grain in (a). (c) TEM bright-field image of the Mg–9.76 wt% Sn alloy aged at 573 K for 5 h to peak hardness. The inset shows a high-magnification image of the particle marked as  $P_1$ . (d) SAED pattern of particle  $P_1$  and the matrix [in (c)] along the  $[001]_\beta//[2\bar{1}\bar{1}0]_\alpha$  direction. (e) Corresponding simulated electron diffraction pattern of (d). Open circles represent  $\beta$ -Mg<sub>2</sub>Sn and filled circles represent  $\alpha$ -Mg. (f) SAED pattern of  $P_1$  and the matrix [in (c)] along the  $[110]_\beta//[01\bar{1}0]_\alpha$  direction. (g) Corresponding simulated electron diffraction pattern of (f). Open circles represent  $\beta$ -Mg<sub>2</sub>Sn and filled circles represent  $\alpha$ -Mg. (h) SAED pattern of particle  $Q_1$  and the matrix [in (c)] along the  $[\bar{1}\bar{1}1]_\beta//[1\bar{2}10]_\alpha$  direction. (i) Corresponding simulated electron diffraction pattern of (h). Open circles represent  $\beta$ -Mg<sub>2</sub>Sn and filled circles represent  $\alpha$ -Mg. (j) TEM bright-field image of the Mg–9.76 wt% Sn alloy aged at 573 K for 5 h, corresponding to its peak hardness, along the  $[0001]_\alpha$  direction. (k) SAED pattern of the matrix [in (j)] along the  $[0001]_\alpha$  direction.



Hence, an atomic structure model of the interface between the  $(220)_\beta$  plane of  $\beta$ -Mg<sub>2</sub>Sn particles with OR-4 and the  $(0001)_\alpha$  plane of the  $\alpha$ -Mg matrix could be constructed and projected along the  $[001]_\beta$  and  $[2\bar{1}\bar{1}0]_\alpha$  directions [inset, Fig. 6(b)]. The proposed atomic model is shown in the inset in Fig. 6(b). The corresponding simulated HRTEM image [inset, small dashed rectangle, Fig. 6(a)] was based on the proposed atomic model and showed agreement with the experimental HRTEM image of the interface between  $\beta$ -Mg<sub>2</sub>Sn particles with OR-4 and the  $\alpha$ -Mg matrix (Fig. 6a).

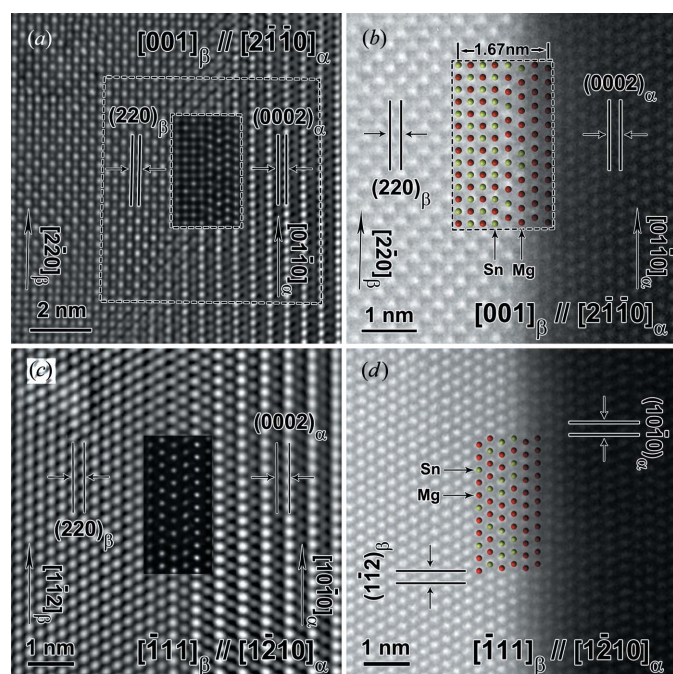
Fig. 6(c) shows an HRTEM image obtained along the same direction as in Fig. 6(a); this image corresponds to the area marked by I in Fig. 4(c). The interface structure between the precipitated  $\beta$ -Mg<sub>2</sub>Sn particle with OR-3 and the  $\alpha$ -Mg matrix could be observed in Fig. 6(c). Fig. 6(d) shows an atomic resolution HAADF-STEM image corresponding to the area in Fig. 6(c). Thus, an atomic structure model of the interface between the  $(220)_\beta$  plane of  $\beta$ -Mg<sub>2</sub>Sn particles with OR-3 and the  $(0001)_\alpha$  plane of the  $\alpha$ -Mg matrix may be proposed and projected along the  $[\bar{1}11]_\beta$  and  $[1\bar{2}10]_\alpha$  directions [inset,

Fig. 6(d)]. Using the atomic structure model shown in Fig. 6(d), the corresponding calculated HRTEM image [inset, Fig. 6(c)] may be obtained, and the results show good agreement with the experimental HRTEM image of the interface between  $\beta$ -Mg<sub>2</sub>Sn particles with OR-3 and the  $\alpha$ -Mg matrix (Fig. 6c). Figs. 6(c) and 6(d) indicate that the  $d$ -value misfits between  $(1\bar{1}2)_\beta$  and  $(10\bar{1}0)_\alpha$ , between  $(220)_\beta$  and  $(0002)_\alpha$ , and between  $(\bar{2}22)_\beta$  and  $(1\bar{2}10)_\alpha$  are 0.71, 8.62 and 19.2%, respectively. Hence,  $\beta$ -Mg<sub>2</sub>Sn particles with OR-3 grow along the  $[1\bar{1}2]_\beta//[10\bar{1}0]_\alpha$  direction. Similarly,  $\beta$ -Mg<sub>2</sub>Sn particles with OR-4 grow along the  $[001]_\beta//[2\bar{1}\bar{1}0]_\alpha$  direction because of the low  $d$ -value misfit (5.18%) between  $(004)_\beta$  and  $(2\bar{1}\bar{1}0)_\alpha$ . Hence,  $\beta$ -Mg<sub>2</sub>Sn particles with OR-3 exhibit longer platelet morphologies than those with OR-4 (Table 2 and Fig. 4j). This result is attributable to the low  $d$ -value misfits of  $\beta$ -Mg<sub>2</sub>Sn particles with OR-3 along the corresponding growth direction.

#### 4. Conclusions

The crystallographic orientation relationships (ORs) of precipitated  $\beta$ -Mg<sub>2</sub>Sn particles in Mg–9.76 wt% Sn alloy aged at 573 K for 5 h, corresponding to its peak hardness, were investigated by advanced TEM. OR-3 of  $(110)_\beta//[0001]_\alpha$  and  $[\bar{1}11]_\beta//[1\bar{2}10]_\alpha$  and OR-4 of  $(110)_\beta//[0001]_\alpha$  and  $[001]_\beta//[2\bar{1}\bar{1}0]_\alpha$  are the key ORs of  $\beta$ -Mg<sub>2</sub>Sn particles in the alloy. The proportions of  $\beta$ -Mg<sub>2</sub>Sn particles exhibiting OR-3 and OR-4 were determined as 75.1 and 24.3%, respectively. Crystallographic factors influenced the predominance of OR-3. The corresponding mechanism was explained by a three-dimensional invariant line model constructed by a measured transformation matrix in reciprocal space. Atomic interface structures between the  $(220)_\beta$  plane of the  $\beta$ -Mg<sub>2</sub>Sn phases with OR-3 and OR-4 and the  $(0001)_\alpha$  plane of the  $\alpha$ -Mg matrix were constructed *via* HRTEM and atomic resolution HAADF-STEM.

This work was supported by the National Natural Science Foundation of China (grant Nos. 51371130, 51171130 and 51271134) and the Fundamental Research Funds for the Central Universities.



**Figure 6**  
 (a) HRTEM image of the area bounded by a dashed lines marked as II in the inset in Fig. 4(c) for the as-cast Mg–9.76 wt% Sn alloy aged at 573 K for 5 h, along the  $[001]_\beta//[2\bar{1}\bar{1}0]_\alpha$  direction. The inset shows a simulated HRTEM image created according to the atomic structure model of the interface. (b) Atomic resolution HAADF-STEM image corresponding to the area enclosed by the large dashed square in (a) along the  $[001]_\beta//[2\bar{1}\bar{1}0]_\alpha$  direction. The inset shows the proposed atomic structure model of the interface between the  $(220)_\beta$  plane of a  $\beta$ -Mg<sub>2</sub>Sn particle with OR-4 and the  $(0001)_\alpha$  plane of the  $\alpha$ -Mg matrix projected along the  $[001]_\beta$  and  $[2\bar{1}\bar{1}0]_\alpha$  directions. (c) HRTEM image of the area bounded by the dashed lines marked as I in Fig. 4(c), along the  $[\bar{1}11]_\beta//[1\bar{2}10]_\alpha$  direction. The inset shows the corresponding simulated HRTEM image. (d) Atomic resolution HAADF-STEM image of the area in (c). The inset shows the proposed atomic structure model of the interface between the  $(220)_\beta$  plane of a  $\beta$ -Mg<sub>2</sub>Sn particle with OR-3 and the  $(0001)_\alpha$  plane of the  $\alpha$ -Mg matrix projected along the  $[\bar{1}11]_\beta$  and  $[1\bar{2}10]_\alpha$  directions.

#### References

Celloto, S. (2000). *Acta Mater.* **48**, 1775–1787.  
 Dahmen, U. (1982). *Acta Metall.* **30**, 63–73.  
 Derge, G., Kommel, A. R. & Mehl, R. F. (1937). *Trans. AIME*, **124**, 367–378.  
 Henes, V. S. & Gerold, V. (1962). *Z. Metallkd.* **53**, 743–748.  
 Hort, N., Huang, Y., Abu Leil, T., Maier, P. & Kainer, K. U. (2006). *Adv. Eng. Mater.* **8**, 359–364.  
 Kang, D. H., Park, S. S. & Kim, N. J. (2005). *Mater. Sci. Eng. A*, **413–414**, 555–560.  
 Kang, D. H., Park, S. S., Oh, Y. S. & Kim, N. J. (2007). *Mater. Sci. Eng. A*, **449–451**, 318–321.  
 Liu, H. M., Chen, Y. G., Tang, Y. B., Wei, S. H. & Niu, G. (2007). *J. Alloys Compd.* **440**, 122–126.  
 Luo, A. A. (2004). *Int. Mater. Rev.* **49**, 13–30.  
 Luo, C. P. & Weatherly, G. C. (1987). *Acta Metall.* **35**, 1963–1972.

- Mendis, C. L., Bettles, C. J., Gibson, M. A., Gorsse, S. & Hutchinson, C. R. (2006a). *Philos. Mag. Lett.* **86**, 443–456.
- Mendis, C. L., Bettles, C. J., Gibson, M. A. & Hutchinson, C. R. (2006b). *Mater. Sci. Eng. A*, **435–436**, 165–171.
- Murray, J. L. (1997). *Alloy Phase Diagrams, ASM Handbook*, edited by H. Baker & H. Okamoto. Materials Park: ASM International.
- Nie, J. F. (2012). *Metall. Mater. Trans. A*, **43**, 3891–3939.
- Nie, J. F., Zhu, Y. M., Liu, J. Z. & Fang, X. Y. (2013). *Science*, **340**, 957–960.
- Sasaki, T. T., Ju, J. D., Hono, K. & Shin, K. S. (2009). *Scr. Mater.* **61**, 80–83.
- Sasaki, T. T., Oh-ishi, K., Ohkubo, T. & Hono, K. (2006). *Scr. Mater.* **55**, 251–254.
- Sasaki, T. T., Oh-ishi, K., Ohkubo, T. & Hono, K. (2011). *Mater. Sci. Eng. A*, **530**, 1–8.
- Shi, Z. Z., Dai, F. Z. & Zhang, W. Z. (2012). *Mater. Sci. Technol.* **28**, 411–414.
- Van Der Planken, J. (1969). *J. Mater. Sci.* **4**, 927–929.
- Wei, S. H., Chen, Y. G., Tang, Y. B., Liu, H. M., Xiao, S. F., Niu, G., Zhang, X. P. & Zhao, Y. H. (2008). *Mater. Sci. Eng. A*, **492**, 20–23.
- Yoon, J. & Park, S. (2014). *Mater. Des.* **55**, 300–308.
- Zhang, M., Zhang, W. Z., Zhu, G. Z. & Yu, K. (2007). *Trans. Nonferrous Metals Soc.* **17**, 1428–1432.
- Zhang, W. Z. & Purdy, G. R. (1993). *Acta Metall.* **41**, 543–551.
- Zheng, O., Zhou, J. P., Zhao, D. S., Wang, J. B., Wang, R. H., Gui, J. N., Xiong, D. X. & Sun, Z. F. (2009). *Scr. Mater.* **60**, 791–794.
- Zhou, J. P., Zhao, D. S., Wang, R. H., Sun, Z. F., Wang, J. B., Gui, J. N. & Zheng, O. (2007). *Mater. Lett.* **61**, 4707–4710.
- Zhou, J. P., Zhao, D. S., Zheng, O., Wang, J. B., Xiong, D. X., Sun, Z. F., Gui, J. N. & Wang, R. H. (2009). *Micron*, **40**, 906–910.